Journal of CO2 Utilization 101 (2025) 103209

Contents lists available at ScienceDirect

Journal of CO2 Utilization

journal homepage: www.elsevier.com/locate/jcou

The impact of heat transfer in packed plasmonic catalyst beds on light-driven CO_2 hydrogenation

Francesc Sastre [a,*], Jonathan van den Ham [a], Jelle Rohlfs [a], Nicole Meulendijks [a], Anthony Sanderse [a], Natalia Mazur [a], Man Xu [a,b], Martin Eschen [a], Alberto Gori [a], Daria Burova [c,d,e], Bjorn Joos [c,d,e], Ken Elen [c,d,e], An Hardy [c,d,e], Marlies K. Van Bael [c,d,e], Pascal Buskens [a,c,**]

[a] The Netherlands Organisation for Applied Scientific Research (TNO), High Tech Campus 25, Eindhoven 5656 AE, the Netherlands
[b] Optics Research Group, Delft University of Technology, Lorentzweg 1 (Building 22), Delft 2628 CJ, the Netherlands
[c] Institute for Materials Research (imo-imomec), DESINe Group, Hasselt University, Agoralaan Building D, Diepenbeek 3590, Belgium
[d] Imomec Associated Laboratory, IMEC vzw, Wetenschapspark 1, Diepenbeek 3590, Belgium
[e] EnergyVille, Thor Park 8320, Genk 3600, Belgium

ARTICLE INFO

Keywords:
FBG-FOS sensors
Plasmonic catalyst
CO2 hydrogenation

ABSTRACT

Fiber Bragg based – fiber optic sensors were applied in operando to monitor the temperature of illuminated plasmonic catalysts at various depths inside the catalyst bed during light-driven CO_2 hydrogenation. Multipoint temperature measurements showed that single-sided illumination induced a pronounced vertical temperature gradient, which remained stable throughout the reaction. This behaviour was observed in two light driven reactions: the exothermic Sabatier reaction catalysed by Ru/Al_2O_3 and the endothermic reverse water gas shift reaction catalysed by Au/TiO_2. The temperature gradient, attributed to a combination of limited light penetration depth and poor thermal conductivity of the catalyst bed, must be taken into account in kinetic studies. Metal loading and gas composition had a strong influence on the temperature gradient, while gas flow rate and reaction heat had a negligible effect. For catalyst temperatures up to 250° C, radiative heat loss accounted for approximately 15 % of the incident light power. Our study demonstrates that accurate in operando temperature monitoring at multiple positions inside the catalyst bed is essential to distinguish between thermal and non-thermal contributors in plasmon catalysis.

1. Introduction

Plasmon catalysis, referring to the utilization of plasmonic nanoparticles for light-driven catalytic processes, emerged around 15 years ago. Seminal work in this field of research include the Au catalyzed steam reforming of ethanol by Psaltis and coworkers [1], Ag catalyzed oxidation of ethylene, CO and NH_3 by the group of Linic [2], Au catalysed oxidation of benzyl alcohol by Scaiano et al. [3] and the plasmon induced H_2 dissociation on Au/TiO_2 by the groups of Halas and Nordlander [4]. Plasmon catalysis utilizes the resonant response of free electrons in metal nanoparticles induced by the electric field of the incident light, called the localized surface plasmon resonance (LSPR) [5]. The LSPR can be tailored by the type of metal, the size, shape and architecture of the metallic nanoparticles, their interparticle distance and the refractive index of the surrounding medium [6]. The LSPR excitation causes a strongly enhanced electromagnetic field at the surface of the nanoparticle [7–12]. Initially excited electrons rapidly thermalize (within 100 fs – 10 ps) and equilibrate via electron-electron scattering, resulting in a hot Fermi-Dirac distribution [13]. Interactions between the hot electrons and phonons of the metal lattice result in an increase of the lattice temperature. In addition to heating with a high degree of spatiotemporal control, two non-thermal effects can also contribute. The first is plasmonic field-driven catalysis, which is based on a resonant energy transfer between the plasmonic nanoparticle and a reactant molecule [13]. This requires an energy overlap between the plasmonic field and the HOMO-LUMO gap of the reactant molecule. In

* Corresponding author.
** Corresponding author at: The Netherlands Organisation for Applied Scientific Research (TNO), High Tech Campus 25, Eindhoven 5656 AE, the Netherlands.
E-mail addresses: francesc.sastrecalabuig@tno.nl (F. Sastre), pascal.buskens@tno.nl (P. Buskens).

https://doi.org/10.1016/j.jcou.2025.103209
Received 21 May 2025; Received in revised form 25 July 2025; Accepted 24 August 2025
Available online 2 September 2025

plasmonic field driven catalysis, the resonant energy transfer forces the atoms of the reactant to reconfigure to accommodate the potential energy surface, which can end with a chemical reaction in the excited state. Alternatively, the reconfigured reactant decays back to the ground state with additional vibrational energy, which lowers the reaction barrier. The second non-thermal contributor is hot carrier-driven catalysis, which implies that plasmon-mediated hot carriers are transferred to an adsorbed molecule [13]. Due to the rapid thermalization of hot electrons, direct transfer to adsorbed molecules is inefficient. The lifetime of hot charge carriers can be significantly prolonged by transferring them to an adjacent semiconductor and trapping them in the semiconductor's conduction band. This spatial separation will prevent hot charge carrier recombination, resulting in the lifetime extension. In conclusion, illuminated plasmonic nanoparticles are efficient nanosources of heat, light and electrons, which can be applied to influence light-driven catalytic chemical processes.

One of the most intensively studied areas of plasmon catalysis is (sun)light-driven catalytic CO_2 hydrogenation, with CH_4 and CO as the two main reported products. Preliminary techno-economic assessments show great potential for sunlight-powered, plasmon catalytic CO and CH_4 production as important processes in the transition of the chemical industry towards climate neutrality [14,15]. CH_4 has been extensively studied by various groups [16–25]. An extensive set of plasmonic catalysts has been reported for the light-driven Sabatier reaction. This reaction is exothermic, claiming that plasmon catalysis lowers its activation barrier and facilitates this reaction under milder conditions when compared to conventional thermal catalysis. Reported plasmonic catalysts include Rh/TiO_2 by Liu and coworkers [26], supported Ni nanoparticles by Sastre et al. [27] and rod-shaped [28] and spherical Ru nanoparticles [25,29] for sunlight-driven CO_2 methanation. Rod-shaped Ru nanoparticle catalyst reached a CH_4 production rate of 52 mmol CH_4 $g_{Ru}^{-1}\cdot h^{-1}$ using sunlight as sole energy source (10.1 $kW\cdot m^{-2}$) [28]. For the spherical Ru nanoparticle catalysts, the highest production rate was 5.09 mol CH_4 $g_{Ru}^{-1}\cdot h^{-1}$ (5.9 % Ru w/w, 6.2 $kW\cdot m^{-2}$ irradiance) [16,29].

CO or syngas (mixture of CO and H_2) is a strategically important target, as its production relies on endothermic reactions such as the reverse water gas shift (rWGS) reaction or dry reforming of methane (DRM). Additionally, syngas is a key feedstock for the synthesis of a wide range of products, including methanol, gasolines and fine chemicals. This production is done via well-established technologies such as Fischer-Tropsch or low-pressure methanol reaction. The production of green syngas will offer a viable pathway to defossilize these industries. In the light-driven rWGS reaction, typical plasmonic catalysts are nanoparticles (NPs) of Au or alloys supported on metal oxides like TiO_2, Al_2O_3, SiO_2 or CeO_{2-x}[30–35]. Without additional heating, the highest CO production rate achieved by our group is 429 $mmol\cdot g_{Au}^{-1}\cdot h^{-1}$[31]. To achieve this reaction rate, the synthetized plasmonic catalyst consisted of 1.5 nm Au NPs with a narrow particle size distribution, supported on pure anatase TiO_2, under 14.4 suns (14.4 $kW\cdot m^{-2}$) solar simulated irradiation. Under light irradiation, the CO selectivity was 98 %. In contrast, the selectivity switched to CH_4 under conventional heating (dark experiments). This phenomenon was attributed to the rapid desorption of CO under illumination, driven by plasmon-induced charges that prevent its further reduction to CH_4. Besides Au/TiO_2, only Au/CeO_{2-x} yielded CO production using light as sole energy source without the need for adding conventional heating. However, the highest reported activity (3.9 $mmol g_{Au}^{-1} h^{-1}$) was two orders of magnitude lower than that of Au/TiO_2.

For DRM, Halas and coworkers reported Cu-Ru alloy NPs as plasmonic catalyst [36]. They reported that the energy efficiency of the process increased with the irradiance of their white light source and reached a maximum of about 15 % at 160 $kW\cdot m^{-2}$, an order of magnitude higher than typical irradiances for the rWGS reaction. Ozin et al. reported a $Ni\text{-}CeO_2\text{-}CePO_4$ nanorod[37]. Under white light irradiation with an intensity of 48.1 $kW\cdot m^{-2}$ and additional heating at 350 °C, they reported an apparent turn over frequency of 1.08×10^{-3} $mol\cdot m^{-2}\cdot h^{-1}$ with low deactivation rates.

Distinguishing between the different contributors to plasmon-mediated reactions, along with accurately quantifying the thermal contribution to plasmon catalytic conversions, and identifying their reaction mechanism is vital for fundamental understanding, rational process development and the successful scale up of this technology. To achieve this, adequate monitoring of the catalyst bed temperature at multiple positions during light irradiation is essential. Typically, thermocouples or IR cameras are used, however these methods have limitations in accuracy. Thermocouples can heat up if they are directly exposed to light, are bulky, and have a relatively large mass compared to the catalyst bed. Additionally, ensuring good thermal contact with the catalyst is challenging. On the other hand, IR thermal cameras only capture the top surface temperature of the catalyst bed and their accuracy depends on the emissivity of the plasmonic catalyst, which varies with the catalyst composition and temperature. To overcome these limitations, we have recently developed fiber Bragg grating-based fiber optic sensors (FBG-FOS). These sensors offers several advantages: they are significantly thinner than thermocouples, have a much lower mass, and do not absorb light. Additionally, multiple FBG-FOS can be positioned at various depths inside the catalyst bed, enabling precise and distributed temperature measurements [38]. This technology is suited for measuring temperature at the microscale, and therefore complementary to spectroscopic techniques like Raman or X-ray absorption fine structure (XAFS), which can be applied to determine surface temperature at the nanoscale [39]. We have previously demonstrated these FBG-FOS for monitoring the temperature of supported plasmonic Ru and Au NP catalysts under light illumination in non-reactive condition (ex situ) [38]. In the present study, we aim to employ FBG-FOS to monitor the temperature of illuminated plasmonic catalyst beds under reaction conditions (in operando), investigating the influence of key parameters such as light intensity, metal loading of the catalyst, feedstock composition and flow speed on the thermal characteristics of the catalyst bed, and their impact on the catalytic process. To elucidate the effect of the reaction heat on the catalyst bed temperature, we have selected one exothermic (Sabatier) reaction and one endothermic (rWGS) reaction as model reactions. These reactions are studied using previously developed spherical Ru/Al_2O_3[29] and Au/TiO_2[30] plasmonic catalysts, respectively, reported by our group. We anticipate that the insights gained from this study will be widely applicable to light-driven plasmon catalytic processes, and contribute to advance the resolution of the ongoing debate on thermal vs. non-thermal contributions.

2. Results and discussion

2.1. Catalyst synthesis and characterization

The two types of catalysts, Ru/Al_2O_3 and Au/TiO_2, were synthesized via thermal decomposition and deposition-precipitation methods, respectively, as described in the experimental section and as previously reported[29,30]. The metal loading was determined by Inductively Coupled Plasma-Atomic Emission Spectroscopy (ICP-AES), yielding a 2.3 wt% and 2.5 wt% loading of Ru and Au, respectively. The size and the shape of the supported NPs were characterized by High-Angle Annular Dark Field - Scanning Transmission Electron Microscopy (HAADF-STEM). Representative images are shown in Fig. 1, Figure S1 and Figure S2. The average Ru and Au particle size and size distribution were determined by measuring at least 250 NPs.

For Ru/Al_2O_3, we observed Ru nanospheres with an average diameter of 0.87 nm randomly distributed of over the Al_2O_3 support (Figure S1c), whereas for Au/TiO_2 the average Au nanoparticle diameter was determined to 2.44 nm (Figure S2). Additionally, for the Ru catalyst, two extra samples with higher Ru loadings were synthesized with Ru content of 3.4 % and 7.8 % with similarly sized Ru NPs (Figure S1). The powder X-ray diffraction (XRD) analysis confirmed the presence of metallic Ru, observed at 38.4°, 42.1°, 44.0°, 69.4°, 78.4°, 82.2°, 84.7°,

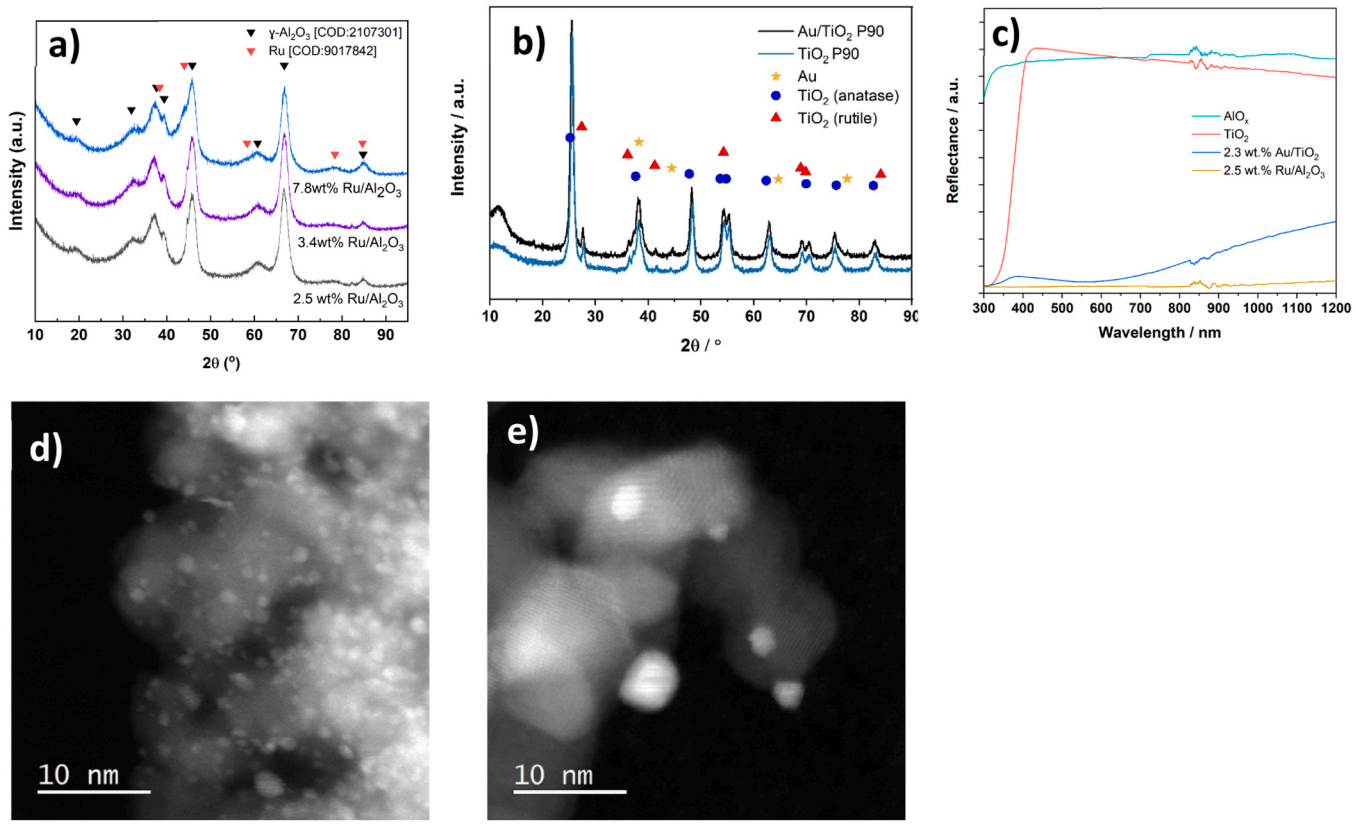

Fig. 1. Catalyst Characterization. a) XRD pattern of the Ru/Al_2O_3 nanocatalyst [Ru COD 9017842, Al_2O_3 COD 2107301; b) XRD pattern of the Au/TiO_2 nanocatalyst [TiO_2 01–073–1764, Au 00–004–0784]; c) Diffuse reflectance UV-Vis-NIR spectra for TiO_2 (red) and Au/TiO_2 (dark blue), Al_2O_3 (light blue) Ru/Al_2O_3 (yellow); d) Representative HAADF-STEM image of the 2.3 wt% Ru/Al_2O_3 catalyst; e) Representative HAADF-STEM image of the Au/TiO_2 catalyst.

and 85.9°, and the γ-Al_2O_3 peaks are displayed at 31.9°, 37.6°, 39.5°, 45.7°, and 66° (Figure S3a). For the Au/TiO_2 catalyst, the diffraction pattern showed peaks at 39.2°, 47.8°, 62.4° and 75.5° attributed to the anatase TiO_2 support and the peaks at 27.4°, 54.26°, 68.9° and 69.8° attributed to the rutile TiO_2 support, and the peaks at 38.2°, 44.4° and 77.7° correspond to metallic Au (Figure S3b). Figure S3c and h show the diffuse UV–visible reflectance spectra for Ru/Al_2O_3 and Au/TiO_2, respectively, displaying a broad absorption band in the range of 300 – 800 nm for both catalysts.

2.2. *Sunlight promoted Sabatier reaction*

To validate the developed FBG-FOS for *in operando* temperature monitoring, and assess the temperature distribution across the catalyst bed, a continuous flow experiment was performed using 2.3 wt% Ru/Al_2O_3 as a plasmonic catalyst under simulated solar light irradiation (7.8 suns) without conventional heating (Fig. 2). CH_4 was the only product detected under light irradiation with a constant production rate of 81.29 $mmol{\cdot}m^{-2}{\cdot}h^{-1}$. Temperature measurements were taken at the catalyst surface (T_{top}) and at a depth of 0.15 mm ($T_{0.15}$) and 0.50 mm ($T_{0.5}$) using three accurately positioned FBG-FOS sensors. Additionally, a thermocouple was placed underneath the quartz filter supporting the catalyst to measure the bottom temperature (T_{bot}). Both the FBG-FOS sensors and the thermocouple were integrated into a catalyst holder previously developed and reported by our group (Figure S3) [38]. When the light was switched on and the catalyst bed illuminated, the catalyst temperature increased rapidly, stabilizing within 3 min. As displayed in Fig. 2, T_{top} reached 191° C, $T_{0.15}$ and $T_{0.5}$ reached 188° C and 180° C, respectively, while T_{bot} reached 115° C. In contrast, the reactor temperature, measured with a thermocouple located 2 cm above the catalyst bed (Figure S4), remained nearly constant at 30° C. When the light was switched off at 125 min, the catalyst temperature decreased rapidly, returning to room temperature within 4 min. Under illumination, the catalyst bed shows a vertical temperature difference of 76° C ($T_{top} - T_{bot}$). This vertical temperature gradient is due to the limited light penetration depth (skin depth) of the catalyst (Figure S4) combined with its poor thermal conductivity. Optical transmission through a gradually increased catalyst layer thickness is measured to determine the light

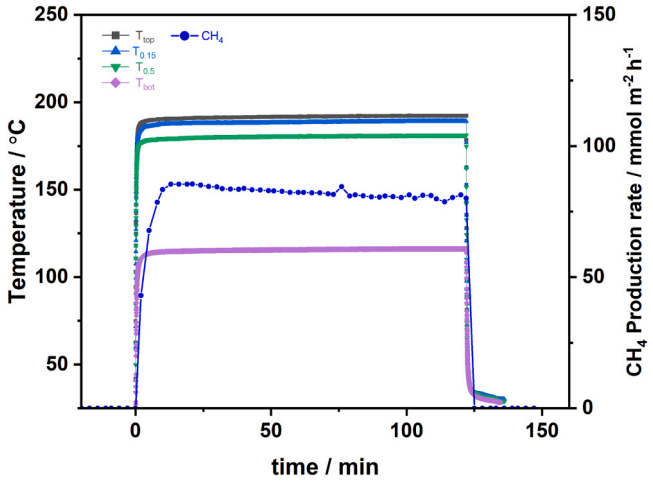

Fig. 2. Catalyst bed temperature and CH_4 production rate as function of time for the CO_2 photomethanation without conventional reactor heating. Reaction conditions: mixture of H_2:CO_2:N_2 (4:1:0.625) with a flow rate of (96:24:15) ml·min^{-1} at 1.5 bar pressure (2.3 wt% Ru/Al_2O_3, 200 mg total catalyst mass, AM1.5 irradiance (7.8 sun = 7.8 kW•m^{-2})).

penetration depth in the catalyst bed. From the transmission the skin depth is determined, as 0.01 % transmission compared to reference. The skin depth of Ru/Al_2O_3 is measured to be 0.02 mm as shown in Figure S3d. In conventionally heated control experiments in dark all the measured temperatures remained uniform at the set point temperature confirming that the thermal gradient is due to the catalyst top illumination. Thermocatalytic experiment in dark at 150 °C was performed resulting in a CH_4 production rate of 82.6 mmol·m^{-2}·h^{-1}. Under these conditions, no vertical temperature gradient across the catalyst bed was observed, as shown in Figure S6.

The relationship between the light irradiance and the catalyst bed temperature was studied for 2.3 % Ru/Al_2O_3 within the range of 3.5–7.8 suns (Fig. 3). Experiments at different light intensities are often carried out in plasmon catalysis to study the relationship between activity and irradiance, which can help to distinguish between thermal and non-thermal contributors[40]. As shown in Fig. 3, the catalyst temperature exhibited a linear increase with increasing irradiance. T_{top} followed a linear rise from 108° C to 196° C as the intensity increased. The vertical temperature gradient across the catalyst bed also became more pronounced under higher irradiance: $T_{top} - T_{0.5}$ increased from 6° C under 3.5 suns to 9° C under 7.8 suns. This effect was even more significant for $T_{top} - T_{bot}$ which increased from 44° C to 88° C. As previously discussed, this gradient is attributed to the shallow skin depth of the plasmonic catalyst and the low thermal conductivity of the porous catalyst bed. The methane production increases exponentially with irradiance, following Arrhenius law. This behaviour indicates the presence of a strong photothermal contributor and supports the previously proposed mechanism [29].

The impact of the Ru loading on the thermal characteristics of the illuminated catalyst bed was studied for 3 different metal loadings. The Ru content, determined by ICP, was 2.3 %, 3.4 % and 7.8 %, respectively. The catalyst bed temperature and methane production rate were studied under 7.8 suns irradiance. As shown in Fig. 4, under identical light irradiation conditions, T_{top} increases by 23° C, rising from 198° C at 2.3 wt% Ru loading to 221° C at 7.8 wt% Ru loading. This indicates that the Ru NPs strongly absorb light resulting in a reduction of skin depth with increasing Ru loading, generating more heat in the top layer of the catalyst bed. In contrast, the Ru loading hardly affects T_{bot}. The vertical temperature gradient $T_{top} - T_{bot}$ increases with increasing Ru loading from 92.3° C for 2.3 wt% Ru loading to 110.9° C at 7.8 wt% Ru loading. The catalytic activity also increases with Ru loading due to the higher number of Ru NPs per m^2 surface area and the enhanced T_{top}. The CH_4 production rate shows exponential increase with the catalyst bed temperature as expected (Fig. 3). The apparent activation energy (E_A) was calculated using the two extreme temperatures measured across the catalyst bed, viz. T_{top} and T_{bot}. When T_{top} was used, an E_A of 75.08 kJ·mol^{-1} was obtained, whereas using T_{bot} yielded an E_A of 95.62 kJ·mol^{-1}. The real E_A lies between these values, emphasizing the importance of accurate temperature measurements.

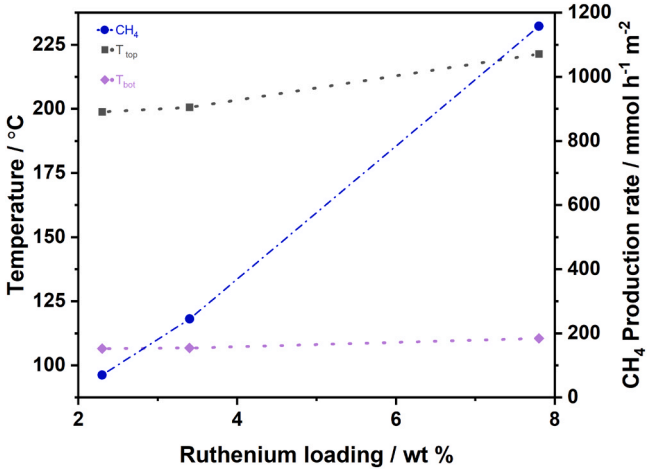

Fig. 4. Catalyst bed temperature and CH_4 production rate as function of Ru loading for the CO_2 photomethanation without conventional reactor heating. Reaction conditions: mixture of H_2:CO_2:N_2 (4:1:0.625) with a flow rate of (96:24:15) ml· min^{-1} at 1.5 bar pressure (2.3 wt% Ru/Al_2O_3, 200 mg total catalyst mass, AM1.5 irradiance (7.8 sun = 7.8 kW•m^{-2})).

To check the influence of feedstock gas composition on the catalyst bed temperature, the reactor was supplied with pure gases (N_2, CO_2, and H_2) as well as with three reaction mixtures with varying H_2:CO_2:N_2 ratios from 4:1:0.62, 1:1:0.25 to –0.25:1:0.15, while maintaining a total constant flow of 135 ml min^{-1}. The catalyst temperature was strongly affected by the gas composition as shown in Fig. 5. T_{top} strongly depended on the gas supplied, increasing 123.6° C when N_2 was used (T_{top} = 278.8° C) instead of H_2 (T_{top} = 155.2° C). These temperature differences can be attributed to the variations in the gas thermal conductivity, as H_2 (0.1805 W·m^{-1}·K^{-1}) [41] has about 7 times higher thermal conductivity than N_2 (0.0258 W·m^{-1}·K^{-1}) [41] and 10 times higher than CO_2 (0.01655 W·m^{-1}·K^{-1}) [41] enabling H_2 to act as an efficient heat

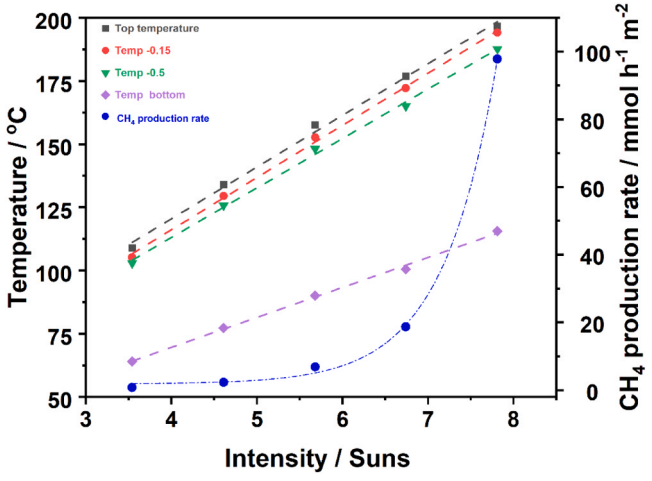

Fig. 3. Catalyst bed temperature and CH_4 production rate as function of light intensity for the CO_2 photomethanation without conventional reactor heating. Reaction conditions: mixture of H_2:CO_2:N_2 (4:1:0.625) with a flow rate of (96:24:15) ml· min^{-1} at 1.5 bar pressure (2.3 wt% Ru/Al_2O_3, 200 mg total catalyst mass, AM1.5 irradiance).

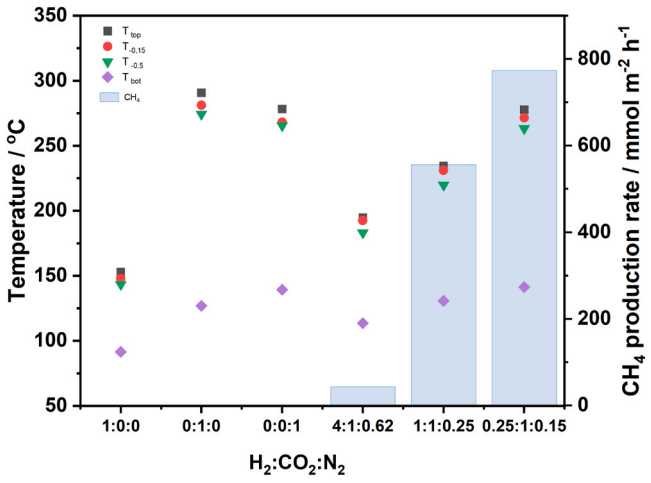

Fig. 5. Catalyst bed temperature and CH_4 production rate as function of feedstock gas composition for the CO_2 photomethanation without conventional reactor heating. Reaction conditions: 1.5 bar pressure (2.3 wt% Ru/Al_2O_3, 200 mg total catalyst mass, AM1.5 irradiance (7.8 sun = 7.8 kW•m^{-2})).

conducting medium in comparison, transporting heat away from the catalyst bed. The supplied gas has a strong effect on the catalyst bed temperature, acting as thermal insulator or heat dissipator. Since pure gases were used, no reaction occurred, meaning that the catalyst bed temperature was not influenced by any reaction heat contributor. When different reaction mixtures were supplied to the reactor, the catalyst bed temperature increased by increasing the CO_2 concentration in the gas reaction mixture. T_{top} increased by 83.1 °C, rising from 194.6 °C with the 4:1:0.62 (H_2:CO_2:N_2) mixture to 277.7 °C with the 0.25:1:0.15 (H_2:CO_2:N_2) mixture. However, T_{bot} presents a lower increase of 27.8 °C as in the previous experiments due to the vertical temperature gradient. The methane production rate increased 8.7 fold from 88.29 $mmol{\cdot}m^{-2}{\cdot}h^{-2}$ to 773.2 $mmol{\cdot}m^{-2}{\cdot}h^{-2}$ as the H_2 fraction in the mixture decreased, leading to a higher catalyst bed temperature. The heat released by the exothermicity of the reaction also increases by the same factor, from 14.57 $kJ{\cdot}\ m^{-2}{\cdot}h^{-1}$ to 127.58 $kJ{\cdot}\ m^{-2}{\cdot}h^{-1}$ which corresponds to just 0.45 % of the total light energy input (28,080 $kJ\ m^{-2}h^{-1}$) and is therefore negligible. To further investigate whether the gas flow direction influenced the catalyst bed temperature, the gas flow was reversed, supplying it from the bottom flowing upward. Similar catalyst bed temperatures were observed regardless of the flow direction, indicating that the flow direction had no significant impact on the achieved temperature (Figure S5).

The influence of the feedstock gas flow on the catalyst bed temperature was studied using pure N_2 and a reaction mixture of H_2:CO_2:N_2 in a 4:1:0.625 ratio. The flow rates supplied to the reactor were varied from 20 % to 200 % of the standard used flow rate (100 % = 135 $ml{\cdot}\ min^{-1}$). The catalyst was irradiated under 7.8 suns. N_2 was used to study the catalyst bed temperature without any possible increase of the catalyst bed temperature coming from the exothermicity of the reaction. As shown in Fig. 6a, when N_2 was used, the catalyst bed temperature remained constant, with only a slight decrease of the catalyst temperature at 200 % flow. This indicates that the gas flow rate has a minimal impact on the catalyst temperature within the studied range. A similar trend was observed under reaction mixture conditions where a stable catalyst temperature was maintained across the flow range achieving a constant methane production rate (Fig. 6b).

2.3. Sunlight promoted rWGS reaction

Finally, to demonstrate that the developed FBG-FOS technology is also applicable to in operando monitoring of endothermic reactions, the light-driven rWGS reaction was selected as a model system. The catalyst bed temperature was investigated at varying irradiance using 2.5 wt% Au/TiO_2 as plasmonic catalyst. The skin depth of this catalyst was 0.10 – 0.12 mm. As previously reported by our group, Au/TiO_2 selectively promotes the CO production. Consistent with the results obtained from the Sabatier reaction, a direct correlation between light intensity and catalyst bed temperature was observed across all measured points in the catalyst bed (Fig. 7). T_{top} increased linearly from 136 °C to 256 °C as the irradiance was raised from 3.5 suns to 7.8 suns. Additionally, the catalysts vertical temperature gradient became more pronounced at higher irradiance. Specifically, $T_{top} - T_{0.5}$ increased from 12.3 °C under 3.5 suns to 20.2 °C under 7.8 suns. These results confirm that the FBG-FOS sensor is capable of accurately monitoring the catalyst temperature in an endothermic light-powered reaction. Furthermore, CO was the only product detected and its production rate followed an exponential increase with the catalyst temperature, consistent with Arrhenius behaviour. This corroborates our previous reported results [30,31]. Also in case of the endothermic rWGS reaction, the impact of the reaction heat is negligible (0.11 % compared to the incident photon flux).

2.4. Radiative heat loss

The intensity of thermal radiation emitted by the catalyst material is described by the Stefan-Boltzmann law. For a Ru/Al_2O_3 catalyst with a

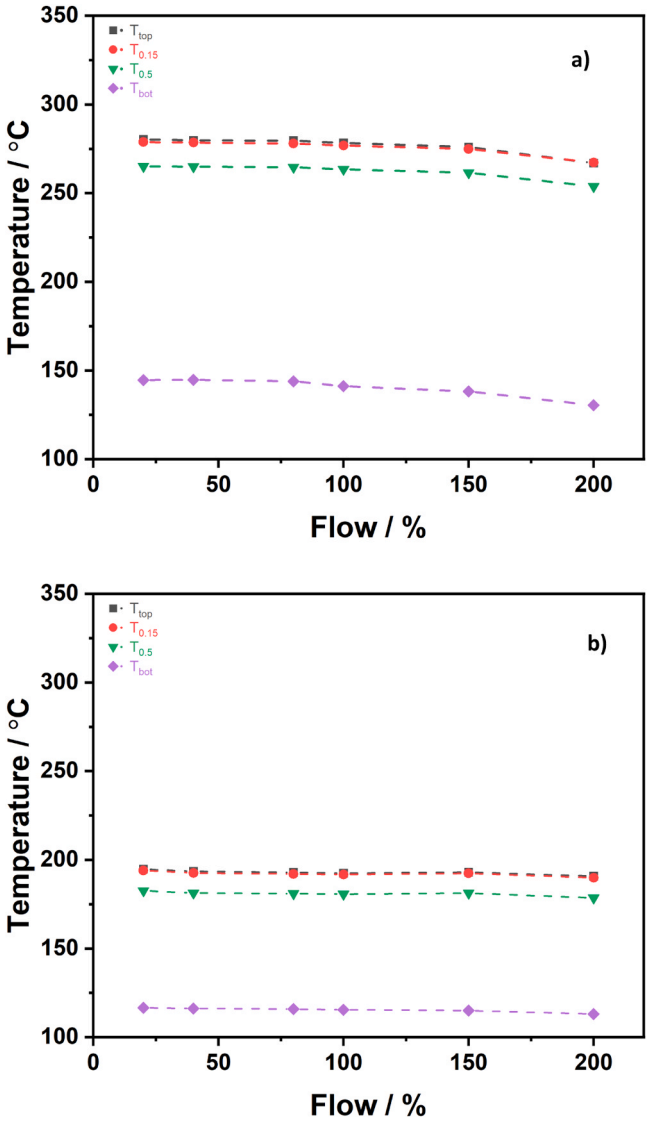

Fig. 6. Catalyst bed temperature as function of total flow: **a)** N_2; **b)** reaction mixture. Reaction conditions: 100 % flow= 135 $ml{\cdot}min^{-1}$ at 1.5 bar pressure (2.3 wt% Ru/γ-Al_2O_3, 200 mg total catalyst mass, AM1.5 irradiance (7.8 sun = 7.8 $kW{\bullet}m^{-2}$)).

Ru loading of 3.4 % w/w, we measured the emissivity as function of temperature between room temperature and 226 °C (Figure S6). At room temperature, the emissivity was above 0.95. With increasing temperature, the emissivity decreased to 0.88 (120 °C), 0.78 (172 °C) and 0.70 (226 °C). This implies that in the temperature range between 120 °C and 226 °C, which is representative for the catalyst bed temperature in the light driven Sabatier reaction, the radiated heat to the top space ranges between 0.59 and 1.23 $kW{\bullet}m^{-2}$. This equals about 15 % of the power of the light source (7.8 $kW{\bullet}m^{-2}$). Similar considerations will apply to the Au/TiO_2 catalyst used for the light powered rWGS reaction, since catalyst temperatures and emissivity are in the same range as for Ru/Al_2O_3. The measured emissivity values for Au/TiO_2 were 0.87 (130 °C), 0.79 (184 °C) and 0.75 (242 °C).

Key implications of the results for plasmon catalysis studies

1. When distinguishing between thermal and non-thermal contributors to light-driven plasmon catalytic conversions, single point temperature measurements of the catalyst bed and thermal reference experiments at a single, uniform catalyst temperature do not suffice. Upon single side illumination, a significant vertical temperature

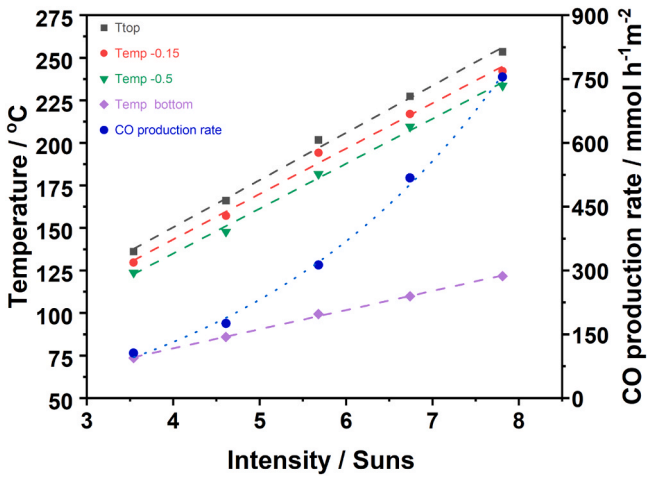

Fig. 7. Catalyst bed temperature and CO production rate as function of light intensity for the light-driven rWGS reaction without conventional reactor heating. Reaction conditions: mixture of H_2:CO_2:N_2 (1:1:0.25) with a flow of (60:60:15) ml·min^{-1} at 1.5 bar pressure (2.5 wt% Au/TiO_2, 200 mg total catalyst mass, AM1.5 irradiance (1 sun = 1 kW•m^{-2})).

gradient occurs, which remains upright during reaction and needs to be taken into account when comparing kinetics of light driven processes to reference experiments in dark.

2. When studying the reaction kinetics of light-driven plasmon catalytic conversions, it is of vital importance to take convective heat losses into account. Systematically changing the concentration of one of the reactants whilst keeping the other reactant concentrations constant results in a significant change of catalyst temperature, which complicates determination of the reaction order and needs to be taken into account.
3. When studying the reaction kinetics of light-driven plasmon catalytic conversions, it is essential to determine the skin depth of the catalyst bed as function of the concentration of metal NPs. Increasing the number of metal NPs not just increases the number of active sites, but typically also reduces the skin depth, localizes heat generation in a thinner layer at the surface of the catalyst bed and changes the top surface temperature and temperature gradient. This effect must be taken into account when performing mechanistic studies of light-driven plasmon catalytic conversions.
4. Radiative heat loss from the catalyst cannot be neglected. Even at relative low catalyst temperatures (up to 250℃), radiative heat loss from the catalyst to the surrounding space above the catalyst is about 15 % of the incoming light power. This radiative heat loss increases exponentially with the temperature, as described by the Stefan-Boltzmann law, and must be considered when further increasing the irradiance. To accurately quantify the radiative heat loss, the emissivity of the catalyst must be determined. Importantly, the emissivity of the catalyst is temperature dependent and should be determined accordingly.

3. Conclusions

The present study demonstrates that FBG-FOS sensors are effective tools for in operando monitoring of the temperature at multiple points inside illuminated plasmonic Ru/Al_2O_3 and Au/TiO_2 catalyst beds. Using these sensors, we identified the presence of a significant vertical temperature gradient in the catalyst bed during the exothermic and endothermic light promoted Sabatier reaction (catalyst = Ru/Al_2O_3) and reverse water gas shift reaction (catalyst = Au/TiO_2), respectively. These gradients must be considered when distinguishing between thermal and non-thermal contributors to light-driven plasmon catalytic conversions. Furthermore, we demonstrated that the temperature gradient is a combined result of the shallow skin depth and poor thermal conductivity of plasmonic catalysts. Whilst metal loading and gas composition strongly influenced the temperature gradient, the impact of gas flow rate and reaction heat was negligible. For catalyst temperatures up to 250℃, the radiative heat loss was about 15 % of the power of the incoming light. These findings highlight the potential that FBG-FOS sensors have for an accurate temperature monitoring and underscore the importance of accurately monitoring both the catalyst's surface temperature and vertical temperature gradient in plasmonic catalysis, both from a fundamental understanding and application and scale up perspective.

4. Photocatalytic tests

The CO_2 photoreduction experiments were performed in a tailored photoreactor system. The reactor was irradiated through a quartz window on top. N_2 was used as internal standard for quantification. The applied light source was a solar simulator (Newport Sol3A) equipped with an AM1.5 filter, with a tunable light intensity up to 7.8 kW·m^{-2} (=7.8 suns). To measure the catalyst bed temperature, a ring was developed with 3 FBG – FOS sensors to measure the temperature distribution inside a plasmonic catalyst bed at 3 different depths in the catalyst bed (Figure S4b). The light attenuation, heat capacity and heat conductivity of FBG-FOS have a negligible influence on photothermal heating and the thermal characteristics of the catalyst bed (Supporting Information, S3). A similar component was previously reported in more detail[38]. The total thickness of the catalyst bed is typically 0.8 mm. The distance between the outmost two fibres is 0.5 mm. The corresponding depths for the 3 sensing points are (T_{top}), at a depth of 0.15 mm ($T_{0.15}$) and 0.5 mm ($T_{0.5}$) using FBG-FOS. Additionally, a thermocouple was placed underneath the quartz filter supporting the plasmonic catalyst to measure the bottom temperature (T_{bot}) (Figure S4a). A scheme of the system is provided in the ESI Figure S4c. The reactor temperature was measured using a second thermocouple (T_r). The standard error of FBG-FOS, including experimental uncertainty, was determined by measuring the catalyst bed temperature in 9 independent experiments. In each experiment, 200 mg of fresh 2.3 wt% Ru/Al_2O_3 catalyst was loaded and irradiated under 7.3 suns in static N_2 conditions. The standard errors of the FBG-FOS were 0.83° C for T_{top} and $T_{0.15}$, and 1.27 ° C for $T_{0.5}$. In the experiments under illumination, simulated sunlight was used as sole energy source without conventional heating of the reactor. Time zero was defined as the moment when the light was switched on.

CRediT authorship contribution statement

Martin Eschen: Investigation, Data curation. **Alberto Gori:** Data curation. **Natalia Mazur:** Writing – review & editing, Methodology, Formal analysis. **Man Xu:** Writing – review & editing, Visualization, Investigation, Formal analysis, Conceptualization. **Pascal Buskens:** Writing – review & editing, Validation, Supervision, Methodology, Funding acquisition, Conceptualization. **Nicole Meulendijks:** Writing – review & editing, Project administration. **Anthony Sanderse:** Writing – review & editing, Formal analysis, Data curation. **An Hardy:** Writing – review & editing. **Jonathan van den Ham:** Writing – review & editing. **Van Bael Marlies K.:** Writing – review & editing. **Jelle Rohlfs:** Formal analysis, Data curation. **Bjorn Joos:** Writing – review & editing. **Ken Elen:** Writing – review & editing. **Francesc Sastre:** Writing – review & editing, Writing – original draft, Visualization, Validation, Supervision, Funding acquisition, Formal analysis, Conceptualization. **Daria Burova:** Data curation.

Declaration of Competing Interest

The authors declare that they have no known competing financial interests or personal relationships that could have appeared to influence

the work reported in this paper

Acknowledgements

This work received funding from the European Union's Horizon 2020 research and innovation programme under grant agreement 101015960 (SPOTLIGHT), the EC Interreg Flanders-The Netherlands project FOTON.

Appendix A. Supporting information

Supplementary data associated with this article can be found in the online version at doi:10.1016/j.jcou.2025.103209.

Data availability

Data will be made available on request.

References

[1] J.R. Adleman, D.A. Boyd, D.G. Goodwin, D. Psaltis, Heterogenous catalysis mediated by plasmon heating, Nano Lett. 9 (2009) 4417–4423, https://doi.org/10.1021/nl902711n.
[2] P. Christopher, H. Xin, S. Linic, Visible-light-enhanced catalytic oxidation reactions on plasmonic silver nanostructures, Nat. Chem. 3 (2011) 467–472, https://doi.org/10.1038/nchem.1032.
[3] J.C. Scaiano, J.C. Netto-Ferreira, E. Alarcon, P. Billone, C.J.B. Alejo, C.-O.L. Crites, M. Decan, C. Fasciani, M. González-Béjar, G. Hallett-Tapley, M. Grenier, K. L. McGilvray, N.L. Pacioni, A. Pardoe, L. René-Boisneuf, R. Schwartz-Narbonne, M. J. Silvero, K.G. Stamplecoskie, T.-L. Wee, Tuning plasmon transitions and their applications in organic photochemistry 83 (2011) 913–930, https://doi.org/10.1351/PAC-CON-11-01-09.
[4] S. Mukherjee, F. Libisch, N. Large, O. Neumann, L.V. Brown, J. Cheng, J.B. Lassiter, E.A. Carter, P. Nordlander, N.J. Halas, Hot electrons do the impossible: Plasmon-Induced dissociation of H2 on au, Nano Lett. 13 (2013) 240–247, https://doi.org/10.1021/nl303940z.
[5] A. Iglesias-Juez, J.M. Coronado, Light and heat joining forces: methanol from photothermal CO2 hydrogenation, Chem 4 (2018) 1490–1491, https://doi.org/10.1016/j.chempr.2018.06.015.
[6] P.K. Jain, M.A. El-Sayed, Plasmonic coupling in noble metal nanostructures, Chem. Phys. Lett. 487 (2010) 153–164, https://doi.org/10.1016/j.cplett.2010.01.062.
[7] G. Baffou, R. Quidant, Nanoplasmonics for chemistry, Chem. Soc. Rev. 43 (2014) 3898–3907, https://doi.org/10.1039/c3cs60364d.
[8] F. Fresno, A. Iglesias-Juez, J.M. Coronado, Photothermal catalytic CO2 conversion: beyond catalysis and photocatalysis, Springe Int. Publ. (2023), https://doi.org/10.1007/s41061-023-00430-z.
[9] Y. Li, Y. Lei, D. Li, A. Liu, Z. Zheng, H. Liu, J. Guo, S. Liu, C. Hao, D. He, Recent progress on photocatalytic CO2 conversion reactions over plasmonic Metal-based catalysts, ACS Catal. 13 (2023) 10177–10204, https://doi.org/10.1021/acscatal.3c02550.
[10] J.C. Scaiano, K. Stamplecoskie, Can surface plasmon fields provide a new way to photosensitize organic photoreactions? From designer nanoparticles to custom applications, J. Phys. Chem. Lett. 4 (2013) 1177–1187, https://doi.org/10.1021/jz400002a.
[11] K. Sytwu, M. Vadai, J.A. Dionne, Bimetallic nanostructures: combining plasmonic and catalytic metals for photocatalysis, Adv. Phys. X 4 (2019), https://doi.org/10.1080/23746149.2019.1619480.
[12] E.A. Coronado, E.R. Encina, F.D. Stefani, Optical properties of metallic nanoparticles: manipulating light, heat and forces at the nanoscale, Nanoscale 3 (2011) 4042–4059, https://doi.org/10.1039/c1nr10788g.
[13] Z. Zhang, C. Zhang, H. Zheng, H. Xu, Plasmon-Driven catalysis on molecules and nanomaterials, Acc. Chem. Res. 52 (2019) 2506–2515, https://doi.org/10.1021/acs.accounts.9b00224.
[14] B. van der Zwaan, R. Detz, N. Meulendijks, P. Buskens, Renewable natural gas as climate-neutral energy carrier? Fuel 311 (2022) 122547 https://doi.org/10.1016/j.fuel.2021.122547.
[15] R. Detz, M. Beerse, N. Meulendijks, P. Buskens, B. van der Zwaan, Towards the use of renewable syngas for the decarbonization of industry, ChemSusChem 17 (2024) 1–10, https://doi.org/10.1002/cssc.202400059.
[16] J. Rohlfs, K.W. Bossers, N. Meulendijks, F.V. Mackenzie, M. Xu, M.A. Verheijen, P. Buskens, F. Sastre, Continuous flow sunlight-powered CO 2 methanation catalyzed by γ -Al 2 O 3 -supported plasmonic Ru nanorods, (2021) 1–11.
[17] P.G. O'Brien, A. Sandhel, T.E. Wood, F.M. Ali, L.B. Hoch, D.D. Perovic, C.A. Mims, G.A. Ozin, Photomethanation of gaseous CO2 over ru/silicon nanowire catalysts with visible and near-infrared photons, Adv. Sci. 1 (2014) 1–7, https://doi.org/10.1002/advs.201400001.
[18] C.M. Rueda-Navarro, M. González-Fernández, M. Cabrero-Antonino, A. Dhakshinamoorthy, B. Ferrer, H.G. Baldoví, S. Navalón, Solar-Assisted CO2 methanation via photocatalytic sabatier reaction by calcined Titanium-based organic framework supported RuOx nanoparticles, ChemCatChem (2024), https://doi.org/10.1002/cctc.202400991.
[19] M. Cabrero-Antonino, B. Ferrer, H.G. Baldoví, S. Navalón, Toward solar-driven photocatalytic CO2 methanation under continuous flow operation using benchmark MIL-125(Ti)–NH2 supported ruthenium nanoparticles, Chem. Eng. J. 445 (2022) 136426, https://doi.org/10.1016/j.cej.2022.136426.
[20] I. García-García, E.C. Lovell, R.J. Wong, V.L. Barrio, J. Scott, J.F. Cambra, R. Amal, Silver-based plasmonic catalysts for carbon dioxide reduction, ACS Sustain. Chem. Eng. 8 (2020) 1879–1887, https://doi.org/10.1021/acssuschemeng.9b06146.
[21] I. Hussain, A.A. Jalil, N.S. Hassan, M.Y.S. Hamid, Recent advances in catalytic systems for CO2 conversion to substitute natural gas (SNG): perspective and challenges, J. Energy Chem. 62 (2021) 377–407, https://doi.org/10.1016/j.jechem.2021.03.040.
[22] S. Khan, X. Dai, T. Ali, S. Mahmood, M. ul Haq, M.S. Riaz, Y. Hu, Recent advances on photo-thermo-catalysis for carbon dioxide methanation, Int. J. Hydrog. Energy 48 (2023) 24756–24787, https://doi.org/10.1016/j.ijhydene.2022.09.224.
[23] A. Quindimil, U. De-La-Torre, B. Pereda-Ayo, A. Davó-Quiñonero, E. Bailón-García, D. Lozano-Castelló, J.A. González-Marcos, A. Bueno-López, J.R. González-Velasco, Effect of metal loading on the CO2 methanation: a comparison between alumina supported ni and ru catalysts, Catal. Today 356 (2020) 419–432, https://doi.org/10.1016/j.cattod.2019.06.027.
[24] P.K. Jain, Comment on "thermal effects-an alternative mechanism for plasmon-assisted photocatalysis" by Y. Dubi, I. W. un and Y. Sivan,: chem. Sci., 2020, 11, 5017, Chem. Sci. 11 (2020) 9022–9023, https://doi.org/10.1039/d0sc02914a.
[25] D. Burova, J. Rohlfs, F. Sastre, P.M. Molina, N. Meulendijks, M.A. Verheijen, A. S. Kelchtermans, K. Elen, A. Hardy, M.K. Van Bael, P. Buskens, Comparing the performance of supported ru nanocatalysts prepared by chemical reduction of RuCl3 and thermal decomposition of Ru3(CO)12 in the Sunlight-Powered sabatier reaction, Catalysts 12 (2022), https://doi.org/10.3390/catal12030284.
[26] X. Zhang, X. Li, D. Zhang, N.Q. Su, W. Yang, H.O. Everitt, J. Liu, Product selectivity in plasmonic photocatalysis for carbon dioxide hydrogenation, Nat. Commun. 8 (2017) 14542, https://doi.org/10.1038/ncomms14542.
[27] F. Sastre, A.V. Puga, L. Liu, A. Corma, H. García, Complete photocatalytic reduction of CO2 to methane by H2 under solar light irradiation, J. Am. Chem. Soc. 136 (2014) 6798–6801, https://doi.org/10.1021/ja500924t.
[28] F. Sastre, C. Versluis, N. Meulendijks, J. Rodríguez-Fernández, J. Sweelssen, K. Elen, M.K. Van Bael, T. Den Hartog, M.A. Verheijen, P. Buskens, Sunlight-fueled, low-Temperature Ru-catalyzed conversion of CO 2 and h 2 to CH 4 with a high Photon-to-Methane efficiency, ACS Omega 4 (2019) 7369–7377, https://doi.org/10.1021/acsomega.9b00581.
[29] R. Grote, R. Habets, J. Rohlfs, F. Sastre, N. Meulendijks, M. Xu, M.A. Verheijen, K. Elen, A. Hardy, M.K. Van Bael, T. den Hartog, P. Buskens, Collective photothermal effect of Al2O3-supported spheroidal plasmonic ru nanoparticle catalysts in the sunlight-powered sabatier reaction, ChemCatChem 12 (2020) 5618–5622, https://doi.org/10.1002/cctc.202000795.
[30] P. Martínez Molina, N. Meulendijks, M. Xu, M.A. Verheijen, T. den Hartog, P. Buskens, F. Sastre, Low temperature Sunlight-Powered reduction of CO2 to CO using a plasmonic Au/TiO2 nanocatalyst, ChemCatChem 13 (2021) 4507–4513, https://doi.org/10.1002/cctc.202100699.
[31] P. Martínez Molina, K.W. Bossers, J.D. Wienk, J. Rohlfs, N. Meulendijks, M. A. Verheijen, P. Buskens, F. Sastre, Sunlight powered continuous flow reverse water gas shift process using a plasmonic Au/TiO2 nanocatalyst, Chem. Asian J. 18 (2023), https://doi.org/10.1002/asia.202300405.
[32] M. Tahir, B. Tahir, N.A.S. Amin, Synergistic effect in plasmonic Au/Ag alloy NPs co-coated TiO2 NWs toward visible-light enhanced CO2 photoreduction to fuels, Appl. Catal. B Environ. 204 (2017) 548–560, https://doi.org/10.1016/j.apcatb.2016.11.062.
[33] J. Volders, K. Elen, A. Raes, R. Ninakanti, A.S. Kelchtermans, F. Sastre, A. Hardy, P. Cool, S.W. Verbruggen, P. Buskens, M.K. Van Bael, Sunlight-Powered reverse water gas shift reaction catalysed by plasmonic Au/TiO2 nanocatalysts: effects of au particle size on the activity and selectivity, Nanomaterials 12 (2022), https://doi.org/10.3390/nano12234153.
[34] A.A. Upadhye, I. Ro, X. Zeng, H.J. Kim, I. Tejedor, M.A. Anderson, J.A. Dumesic, G. W. Huber, Plasmon-enhanced reverse water gas shift reaction over oxide supported au catalysts, Catal. Sci. Technol. 5 (2015) 2590–2601, https://doi.org/10.1039/c4cy01183j.
[35] B. Tahir, M. Tahir, N.S. Amin, Gold-indium modified TiO 2 nanocatalysts for photocatalytic CO 2 reduction with h 2 as reductant in a monolith photoreactor, Appl. Surf. Sci. 338 (2015) 1–14, https://doi.org/10.1016/j.apsusc.2015.02.126.
[36] L. Zhou, J.M.P. Martirez, J. Finzel, C. Zhang, D.F. Swearer, S. Tian, H. Robatjazi, M. Lou, L. Dong, L. Henderson, P. Christopher, E.A. Carter, P. Nordlander, N. J. Halas, Light-driven methane dry reforming with single atomic site antenna-reactor plasmonic photocatalysts, Nat. Energy 5 (2020) 61–70, https://doi.org/10.1038/s41560-019-0517-9.
[37] A. Tavasoli, A. Gouda, T. Zahringer, Y.F. Li, H. Quaid, C.J. Viasus Perez, R. Song, M. Sain, G. Ozin, Enhanced hybrid photocatalytic dry reforming using a phosphated Ni-CeO2 nanorod heterostructure, Nat. Commun. 14 (2023) 1–8, https://doi.org/10.1038/s41467-023-36982-3.
[38] M. Xu, T. den Hartog, L. Cheng, M. Wolfs, R. Habets, J. Rohlfs, J. van den Ham, N. Meulendijks, F. Sastre, P. Buskens, Using fiber bragg grating sensors to quantify temperature Non-Uniformities in plasmonic catalyst beds under illumination, ChemPhotoChem 6 (2022), https://doi.org/10.1002/cptc.202100289.
[39] S. Liu, Z. Wu, Z. Zhu, K. Feng, Y. Zhou, X. Hu, X. Huang, B. Zhang, X. Dong, Y. Ma, K. Nie, J. Shen, Z. Wang, J. He, J. Wang, Y. Ji, B. Yan, Q. Zhang, A. Genest, X. Zhang, C. Li, B. Wu, X. An, G. Rupprechter, L. He, Quantifying the distinct role of

plasmon enhancement mechanisms in prototypical antenna-reactor photocatalysts, Nat. Commun. 16 (2025) 1–12, https://doi.org/10.1038/s41467-025-57569-0.
[40] Z. Zhu, R. Tang, C. Li, X. An, L. He, Promises of plasmonic Antenna-Reactor systems in Gas-Phase CO2 photocatalysis, Adv. Sci. 10 (24) (2023) 1, https://doi.org/10.1002/advs.202302568.
[41] D.W. Green, M.Z. Southard, D.W. Green, M.Z. Southard (Eds.), Perry's chemical Engineers' Handbook, 9th ed., McGraw-Hill Education, New York, 2019. ⟨https://www.accessengineeringlibrary.com/content/book/9780071834087⟩.